

## Numerical Study of Flow Structures Through Horizontal Double-Layered Vegetation Consisting of Combined Submergent and Emergent Vegetations

Fakhar Muhammad Abbas

*Graduate School of Science and Engineering  
Saitama University, 255 Shimo-okubo, Sakura-ku  
Saitama-shi, Saitama 338-8570, Japan  
abbasfakhar103@gmail.com*

Norio Tanaka\*

*International Institute for Resilient Society  
Saitama University, 255 Shimo-Okubo, Sakura-ku  
Saitama-shi, Saitama 338-8570, Japan  
tanaka01@mail.saitama-u.ac.jp*

Received 2 July 2021

Accepted 23 December 2021

Published 30 March 2022

This study addresses the vivid internal flow structure variations through horizontal double-layered vegetation (HDLV) under subcritical flow conditions for an inland tsunami. The computational domain was built in ANSYS Workbench, while post-processing and simulation were performed using the computational fluid dynamics (CFD) tool FLUENT with the three-dimensional (3D) Reynolds stress model (RSM). Two alternative arrangements of HDLV were considered, namely Configuration 1 (short submergent layer ( $L_s$ ) + tall emergent layer ( $L_t$ )) and Configuration 2 (tall emergent layer ( $L_t$ ) + short submergent layer ( $L_s$ )) along with varying flow depths. Strong inflections in velocity and Reynolds stress profiles were observed at the interface near the top of  $L_s$ . Whereas, these profiles were almost constant from bed to the top of vegetations inside  $L_t$ . A shear layer zone was formed above the top of  $L_s$ , which extended to the downstream region in Configuration 2 while it was restricted by  $L_t$  in Configuration 1. The normal Reynolds stresses at the bed were significantly greater within  $L_s$  in Configuration 2 than inside  $L_t$  in Configuration 1. Hence, Configuration 1 was performed relatively better than Configuration 2 in terms of reducing velocity within the vegetation, while Configuration 2 played a key role in attenuating the increased velocities and confining the shear layer above the short submergent layer.

**Keywords:** Horizontal double-layered vegetation; tsunami; Reynolds stress model; Fluent; velocity structure; Reynolds stresses.

\*Corresponding author.

## 1. Introduction

A huge tsunami is considered to be one of the most terrible natural disasters and causes enormous catastrophic demolition of socio-economic property and loss of human lives [Mori and Takahashi, 2012]. At the start of the 21st century, two overwhelming tsunamis (2004 Indian Ocean, 2011 Great East Japan) occurred and caused catastrophic destruction [Danielsen *et al.*, 2005; Tanaka *et al.*, 2013]. After these megadisasters, the need for protective measures against a tsunami was realized. Many hard and soft solutions including artificial (hydraulic structures) and natural structures (coastal vegetations) were proposed for tsunami mitigation [Tanaka *et al.*, 2014]. The construction of artificial structures may be expensive for developing countries because it requires a large financial investment [Tanaka, 2009]. Thus, the importance of natural structures, such as coastal vegetations, has attracted the attention of researchers because they are considered to be an effective source of tsunami mitigation and provide an ecofriendly environment [Kathiressan and Rajendran, 2005; Osti *et al.*, 2009; Yanagisawa *et al.*, 2009, 2010]. The use of coastal vegetation as a tsunami countermeasure depends upon different factors including density [Harada and Kawata, 2005; Irem *et al.*, 2009], species, dimensions, alignments, and scale of the vegetations [Thuy *et al.*, 2010]. Iimura and Tanaka [2012] investigated the impact of tree vegetation density and found that the increment of vegetation density reduces the water level and velocity on the downstream side of the vegetation. Similarly, according to Pasha and Tanaka [2017], dense emergent vegetation is more feasible for inland tsunami mitigation than sparse emergent vegetation. During a survey after the 2004 Indian Ocean Tsunami (IOT) in Sri Lanka, a vertically double-layered coastal vegetation comprising of *P. odoratissimus* (short trees) and *C. equisetifolia* (tall trees) was proved as an effective countermeasure against tsunami. Because *P. odoratissimus* has dense aerial roots, it is effective to reduce the tsunami force when the tsunami height is less than 5 m [Tanaka *et al.*, 2007]. *C. equisetifolia* trees become tall with a large trunk diameter. Therefore, many researchers have devoted their attention to clarify the effectiveness of a vertically double-layered vegetation (VDLV) (short within tall trees) in their experimental [Rashedunnabi and Tanaka, 2019, 2020; Anjum and Tanaka, 2019a] and numerical studies [Anjum and Tanaka, 2019b]. They concluded that this type of vertically double-layered arrangement has great potential as a bio-shield against tsunamis, but it is difficult to grow the denser short trees, i.e. *P. odoratissimus*, among the tall trees (*C. equisetifolia*) because the tall trees require sufficient space to grow well. As a result, due to lack of space for effective growth of tall emergent trees, this study introduced the combination of a horizontal double layer of dense short trees as the first row, with the sparse tall trees as the second row (i.e. HDLV), and then changed the order of these two tree combinations one by one. Previously, a numerical study conducted by Samarakoon *et al.* [2012] used the combination of short trees (*P. odoratissimus*) as a front layer to minimize the disadvantage of open gaps (like a road or river) among the existing tall trees (*C. equisetifolia*). However, no studies on

the use of this form of horizontal double-layered vegetation (HDLV) as a counter-measure against tsunamis in inland locations have been reported yet. That is why it is essential to analyze the detailed flow structure through HDLV against an inland tsunami flow and to compare it with previous research work. A coastal forest has the power to limit tsunami energy; therefore, protecting an inland coastal zone with a natural defensive mechanism such as vegetation is essential. Thus, the goal of this research was to analyze the internal flow pattern in terms of a detailed three-dimensional (3D) velocity structure and other flow properties of tsunami flows approaching inland via a coastal vegetation HDLV in precise detail. Furthermore, the flow structure within the vegetation cylinders is difficult to capture in an experimental study due to the limitations of instrument use within the vegetation area, such as the use of an electromagnetic flowmeter (EFM) or a particle image velocity meter (PIV) for velocity measurement and a shear stress meter (SSM) for measuring bed shear stresses. One of the benefits of the current numerical research was that it was able to overcome this obstacle. To accomplish the goal, a numerical analysis was undertaken using two vegetation configurations, the first of which was a short-submerged layer on the upstream side with a tall emergent layer on the downstream side, and the second of which was a tall emergent layer on the upstream side with a short-submerged layer on the downstream side. The main objectives of this study are as follows:

- (1) Analysis of the detailed flow structure in terms of 3D velocity structure and Reynold's stress distribution around the HDLV model by using the Reynold's stress model.
- (2) Elucidation of the effects of varying the flow depths through HDLV, and
- (3) Comparison of the effects of the two configurations of HDLV model considered on the resulting flow patterns.

## 2. Modeling Approach

### 2.1. *Experimental setup for validation of numerical model*

The present numerical model was validated by utilizing the experimental data of Liu *et al.* [2010]. The experimental setup was conducted in a laboratory flume having a Plexiglass flume (length = 4.3 m, width = 0.3 m) with a constant slope of 0.003. The VDLV model consisted of tall vegetation (15 cm) with short vegetation (5.1 cm) inserted into the staggered arrangement as an array of rigid cylinders with a diameter ( $d$ ) of 0.635 cm. The VDLV model covered a length of 3 m and width of 0.3 m fixed at a distance of 1.3 m from the upstream inlet. The spacing of tall and short cylinders was selected based on the non-dimensional parameter  $Ss/d$  and  $St/d$  for short and tall cylinders (where  $Ss = 5d$  represents spacing between short cylinders and  $St = 10d$  represents spacing between tall cylinders). Instantaneous measurements of velocity were obtained at 2.25 m downstream from the start of the section, assuring that the flow was fully developed. The mean flow was measured using a

one-dimensional laser Doppler velocimeter. The flow depth and discharge rate selected were 0.121 m and  $1.140 \times 10^{-2} \text{ m}^3/\text{s}$ , respectively. In addition, the Reynolds number ( $Re$ ) and initial Froude number ( $Fr$ ) selected were 37300 and 0.2820 m.

## 2.2. Computational model setup

To reduce the computational cost, there is a need to simplify the domain length of the experimental setup. Thus, only the domain of the vegetated portion (length 0.6 m; width 0.3 m) was considered for modeling in ANSYS Workbench, while the other flow variables were kept constant. The whole numerical domain for validation is presented in Figs. 1(a) and 1(b). Rigid solid circular cylinders were used to achieve flow interaction. Multizone meshing along with hexagonal elements was used in this numerical modeling. To verify the quality of the simulation mesh skewness, an independence test and orthogonal quality criterion were also included. Skewness is considered a primary factor to judge the quality of the mesh. Skewness can be defined as is how closely the face or cell resembles the ideal. A “0” value of skewness is “excellent”, while “1” is an indication of the worst quality of a cell or face. In the current numerical domain, the equilateral volume-based method was applied to check skewness. According to this method, the best quality 3D meshing should have

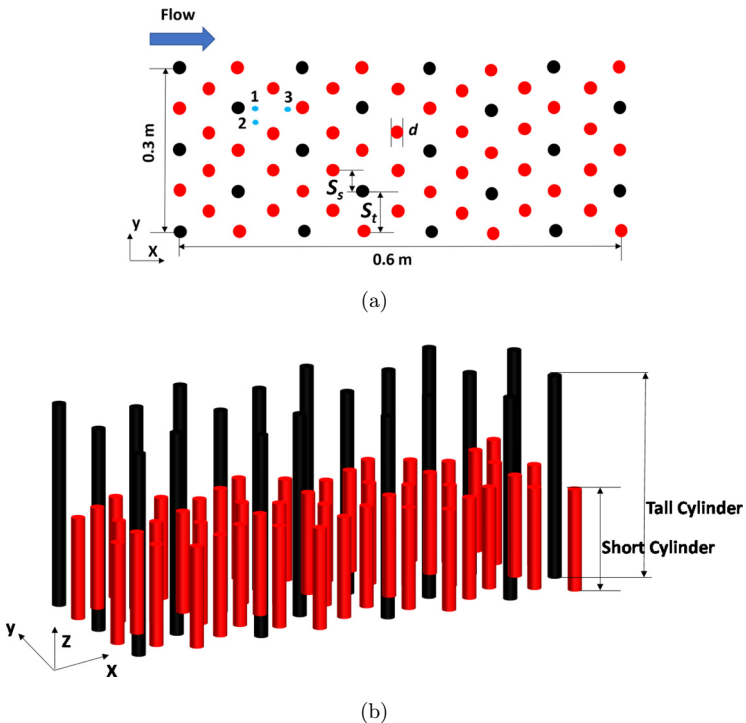


Fig. 1. (a) Numerical domain (a) Top view of domain and specified locations and (b) 3-dimensional layout.

a value of approximately 0.15. The current mesh geometry had a value of skewness between 0.14–0.19, which indicates excellent mesh quality. Second, the orthogonal criterion applied was “0 for worst” and “1 for good”. Thus, the value of the orthogonal criterion for the present meshed body was 0.98, which indicates an approximately good quality mesh.

To obtain the translational periodicity and uniform flow features, the periodic boundary condition was applied at the inlet/outlet. The mass flow rate of  $1.140 \times 10^{-2} \text{ m}^3/\text{s}$  was set at the periodic boundary. For the top free surface, a symmetrical boundary condition was utilized. A non-slip wall condition was applied to the edge of the cylinder and bed of the domain. The computational fluid dynamics (CFD) program Fluent including a 3D Reynolds stress model (RSM) was utilized for post-processing and simulation. Under-relaxation factor values were considered to be low for convergence criteria and residual smoothing. The standard initialization method was used for solution initialization.

### 2.3. Validation of computational model

The computed streamwise velocity profiles at specified points were compared with the experimental results of Liu *et al.* [2010] to certify the validity of the computational model in Fig. 2. The velocity is depicted on the  $x$  axis and normalized by the shear velocity ( $u_* = (ghS)^{\frac{1}{2}}$ , where  $g$  is the gravitational constant,  $h$  is the flow depth, and  $S$  is the slope), whereas the  $y$  axis depicts the depth of flow and is normalized by the short vegetation height ( $h_s$ ). The computed and experimental results show that the velocities observed at point 2 in the gap region were higher than the velocities observed at points 1 and 3, which were located in between the short and tall cylinders. The computed results show a close resemblance and good correspondence to the experimental results. They indicate the validity of the numerical model,

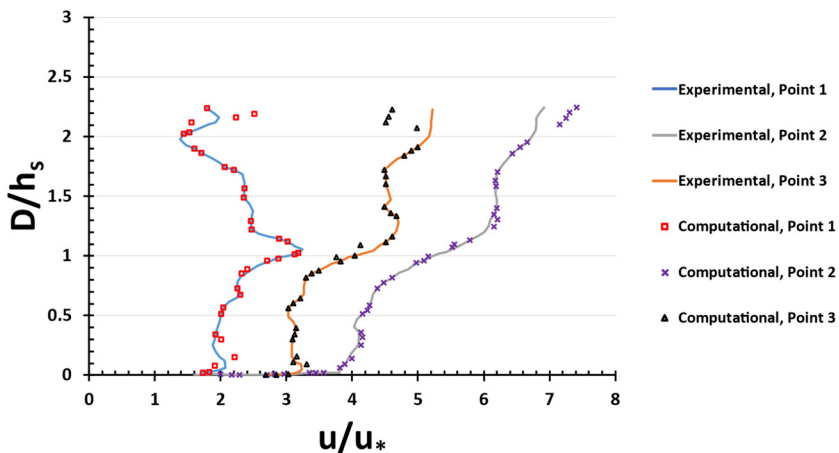


Fig. 2. Comparison between computational and experimental results.

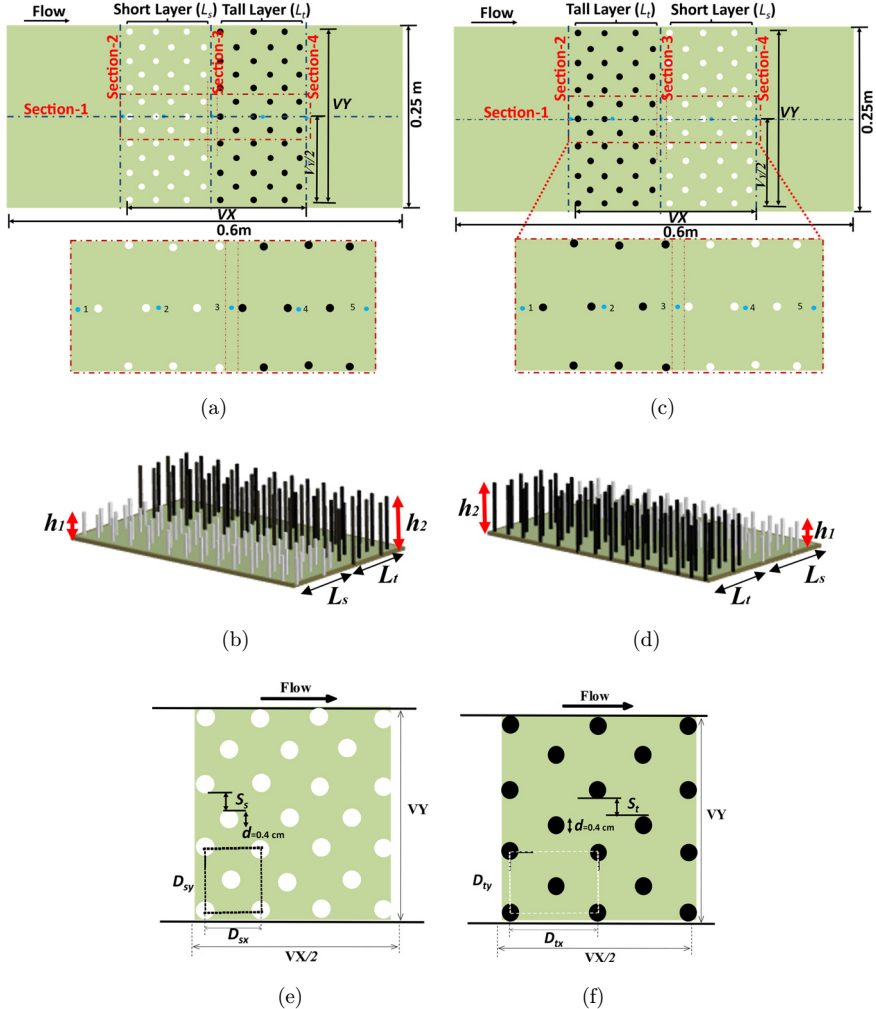


Fig. 3. Schematic of numerical domain along with specified locations. (a) For vegetation Configuration 1, (b) isometric view for Configuration 1, (c) for vegetation Configuration 2, (d) isometric view for Configuration 2, (e) spacing between short cylinders, and (f) spacing between tall cylinders.

and that the model can capture better results. However, near the free surface level, i.e.  $2.00 < D/h_s < 2.3$ , there is a small difference between the computed and experimental findings. This may be due to the assignment of the symmetry boundary condition to the top free surface in the present numerical geometry because it treats the upper free surface as a flat boundary. Second, in the actual flow, the water level difference within the vegetation caused a pressure difference, and due to this pressure difference, the velocity at the free surface level is increased [Roulund *et al.*, 2005; Wang *et al.*, 2014; Anjum and Tanaka, 2019b]. The internal velocity structures can

examine the concerning validation requirements such as the symmetrical boundary condition, despite modest deviations near the water surface.

## 2.4. Computational model for present study

### 2.4.1. Flow conditions

In the 2011 Great East Japan Tsunami (GEJT), the tsunami flow surrounding an inland forest in Miyagi Prefecture, Japan, was subcritical at several sites with Froude numbers ranging from 0.7 to 1 and an estimated tsunami inundation depth of 7.3–8.3 m [Tanaka *et al.*, 2013]. During the IOT of 2004, the *Fr* numbers were estimated to be 0.64–1.04 in the inland area in Banda Aceh [Fritz *et al.*, 2006]. Therefore, a model scale of 1/100 and two flow conditions were selected to simulate a tsunami flow on a real scale while maintaining the Froude number. Hence, the initial Froude number ( $Fr = \frac{u}{\sqrt{gh}}$ ) was defined by the values of the water depth and velocity without considering a vegetation model in the channel. The water depths (without a vegetation model) used in this numerical study for establishing the subcritical inland tsunami conditions were 6 and 8 cm, respectively, giving the initial Froude numbers to be 0.67 and 0.70.

### 2.4.2. Vegetation model conditions

In the Sendai Plain, the vegetation density, diameter, and trunk height were estimated as 0.2 trees/m<sup>2</sup>, 0.4 m, and 15 m, respectively [Tanaka and Onai, 2017]. Tanaka *et al.* [2007] showed that following the 2004 IOT, *C. equisetifolia* trees with a trunk diameter of more than 0.3 m placed in the front line of vegetation in Sri Lanka were unbroken and capable of trapping man-made debris and broken branches of trees. Furthermore, the research also showed that the trees having large trunk diameters were found in areas with sparse tree density (more space between trees). Another vegetation species, i.e. *P. odoratissimum* has been proven to be beneficial due to its dense arrangement and complicated aerial roots [Jayatissa *et al.*, 2002], which also affect the drag coefficient [Wolanski *et al.*, 1980; Tanaka *et al.*, 2007] for protection from the tsunami flow. In the 2004 IOT, *P. odoratissimum* trees were found in many areas, and residents living behind these forests were only marginally affected. Furthermore, *P. odoratissimum* is more effective when the tsunami height is less than 5 m [Tanaka *et al.*, 2007]. A study conducted by Samarakoon *et al.* [2012] suggested that planting *P. odoratissimum* in front of *C. equisetifolia* trees reduced the drawbacks of open gaps (like a road or a river in a forest) more efficiently than planting *M. hexandra* trees at the rear of *C. equisetifolia* vegetation. Thus, the profile of a *P. odoratissimum* tree can be scaled down to a solid circular cylinder by taking into account the thick roots and the trunk diameter at breast height [Thuy *et al.*, 2018].

Therefore, in the present numerical study, the horizontal double layer vegetation HDLV model was considered with the first configuration comprising a half layer of short trees (*P. odoratissimum*) and a half layer of the tall trees (*C. equisetifolia*) and

then the order of the trees was changed in the second configuration. The density of the tall trees adopted was low so that the crown part of the tree was comparatively higher than the flow depth and the short trees. As a result, only the remaining trunk part of the tall tree provided resistance, which was represented by solid circular cylinders, against the tsunami current, whereas the density of the short trees was based on the dense *P. odoratissimus* tree growth.

A tree may be broken in actual tsunami conditions. However, tree breakage was not considered in this study to investigate the flow structure variation through the horizontal double layer vegetation HDLV model. The diameter of the solid circular cylinder was selected based on non-breaking tree trunk diameter ( $d > 40$  cm) [Tanaka *et al.*, 2013]. Therefore, based on the model scale of 1/100, the diameter ( $d$ ) selected to simulate the tree cylinder in the numerical modeling was 0.004 m. The short tree height ( $h_1$ ) was fixed at 5 cm to reflect the high density and short height of *P. odoratissimus* trees, whereas the tall tree height ( $h_2$ ) was fixed at 18 cm to reflect the trunk of the *C. equisetifolia* trees.

The vegetation density is defined by the  $S/d$  value [Takemura and Tanaka, 2007]. This  $S/d$  number defines that whether the vegetation model is sparse, intermediate, or dense, where  $S$  represents the clear spacing between the located cylinders in a crosswise flow, and  $d$  depicts the diameter of the cylinder. An  $S/d$  value of 2.15 represents a sparse arrangement, while the values of 1.03 and 0.25 depict intermediate and dense arrangements, respectively. In this study, two  $S/d$  values were selected as 0.0425 and 2.15 for short cylinders (submerged) and tall cylinders (emergent), respectively, based on previous research [Pasha and Tanaka, 2017].

The present domain was modeled by a rectangular channel of 0.6 m long and 0.25 m wide comprising a HDLV covering the full width of the domain with two different configurations. The first configuration consisted of the combination of a short submerged layer ( $L_s$ ) as the front layer and a tall emergent layer ( $L_t$ ) as the back layer, while the second configuration comprised  $L_t$  as the front layer and  $L_s$  as the back layer. Finally, four cases were selected based on the flow depths and configuration types. The hydraulic conditions and vegetation conditions for the selected cases are shown in Tables 1 and 2, respectively. In Table 2,  $d$ ,  $h_1$ , and  $h_2$  depict the diameter and heights of short and tall cylinders, respectively. The symbols  $D_{sy}$  and

Table 1. Hydraulic conditions.

Case no.	Vegetation type	$Q$ ( $10^{-3} \text{ m}^3/\text{s}$ )	$Z$ (cm)	$Fr$	$Re^*$	$Re$
1	Dense Short- $L_s$ Sparse Tall- $L_t$	9.4	6	0.67	2048	30717
2	Sparse Tall- $L_t$ Dense Short- $L_s$	14.9	8	0.7	2471	49410
3	Dense Short- $L_s$ Sparse Tall- $L_t$	9.4	6	0.67	2048	30717
4	Sparse Tall- $L_t$ Dense Short- $L_s$	14.9	8	0.7	2471	49410

*Notes:*  $Q$  represents the discharge value of the flow;  $Q = A \cdot V$ , where  $A$  is the cross-sectional area and  $V$  is the flow velocity;  $Z$  is the flow depth;  $Fr$  is the initial Froude number against the flow depth  $Z$ ;  $Re^* = Vd/\eta$  depicts the Reynolds number of cylinders where  $\eta$  shows the water viscosity and  $d$  shows the diameter of the cylinder and  $Re = VZ/\eta$  is the Reynolds flow number.

Table 2. Geometric conditions of vegetation for computational domain.

Vegetation type	$d$ (cm)	$h_1$ (cm)	$h_2$ (cm)	$D_{sy}$ (cm)	$D_{ty}$ (cm)	$S_s$ (cm)	$S_t$ (cm)	$S_s/d$	$S_t/d$
Dense Short- $L_s$	0.4	5	—	0.83	—	0.017	—	0.0425	—
Sparse Tall- $L_t$	0.4	—	18	—	2.5	—	0.85	—	2.125

$D_{ty}$  show the spacing between the center-to-center of short and tall cylinders, respectively, in the lateral direction, and  $S_s$  and  $S_t$  represent the spacing between cylinders in which subscripts  $s$  and  $t$  represent short and tall trees.

The boundary conditions applied to the whole domain were the same as those adopted for the validation model. The isometric view and spacing between cylinders and arrangement are described in Figs. 3(a)–3(f). To investigate and visualize the comprehensive physics of flow, Sec. 1 was aligned longitudinally along the center of the numerical domain. In contrast, Secs. 2–4 were aligned laterally up-, mid-, and downstream of vegetation patches, respectively, to investigate the behavior of stream-, span-, and depth-wise velocities, whereas the behavior of Reynolds stresses was scrutinized at location 1 (upstream of the patch), location 5 (downstream of vegetation patch), and locations 2–4 (inside the vegetation patch), as shown in Figs. 3(a) and 3(c).

### 3. Results and Discussion

#### 3.1. Longitudinal distribution of velocities profiles

##### 3.1.1. Longitudinal distribution of streamwise velocities

The computed results of the longitudinal distribution of streamwise velocity profiles ( $u$ ) along Sec. 1 for all four cases are presented in Figs. 4(a)–4(d). The  $x$  axis represents the length of the computational domain while the  $y$  axis depicts the longitudinal velocity ( $u$ ), which is normalized by the initial velocity ( $U$ ). The yellow and blue dotted boxes represent the locations of short and tall vegetation cylinders, respectively. To investigate the internal flow structure within HDLV, three lines were considered at different depths: (i) Near the bed region ( $Z/h_1 = 0.7$ ), (ii) at the top of the short submerged vegetation ( $Z/h_1 = 1$ ), and (iii) close to the free surface region ( $Z/h_1 = 1.2$  for flow depth  $Z = 6$  cm) and ( $Z/h_1 = 1.4$  for flow depth  $Z = 8$  cm) in Sec. 1 located longitudinally at the middle of the channel. The non-dimensionalized streamwise velocities ( $u/U$ ) were almost uniform upstream and downstream of the vegetation patch, as shown in Figs. 5(a) and 5(b) considering Configuration 1, where the first half layer was a short layer ( $L_s$ ) and the remaining half layer was a tall layer ( $L_t$ ) against the considered flow depths, whereas the opposite trend of streamwise velocities was observed, especially on the downstream side of the vegetation model in Configuration 2 of Figs. 4(c) and 4(d), in which the first half layer considered was tall and the remaining half layer was short. The velocities were increased at the downstream side in vegetation of Configuration 2.

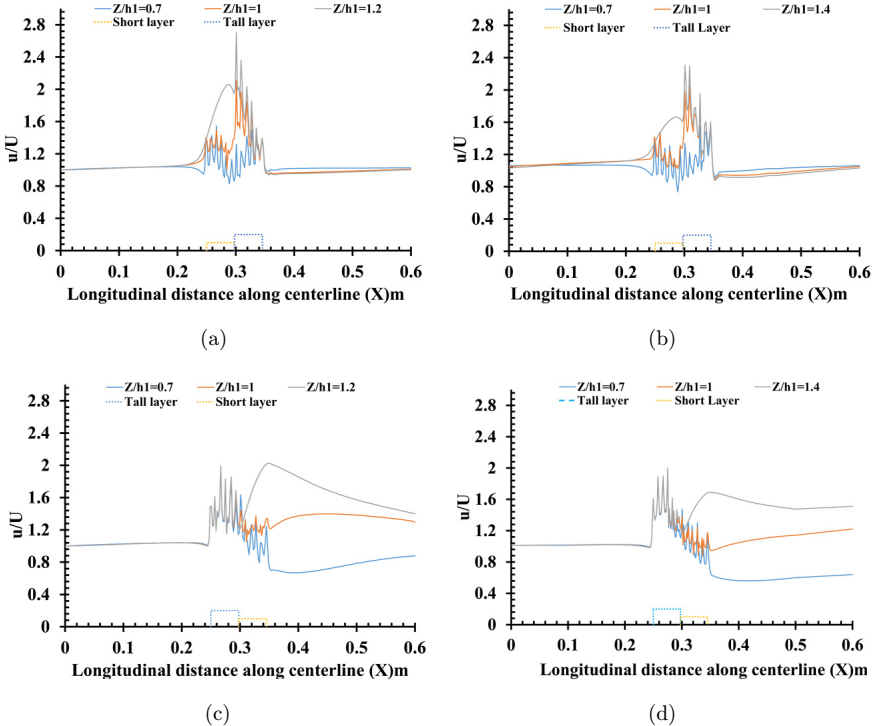


Fig. 4. Longitudinal distribution of streamwise velocities profiles along Sec. 1. (a) Case 1, (b) Case 2, (c) Case 3, and (d) Case 4.

It was due to the difference in velocities between the submerged vegetation region and the overlying flow layer, which generates a sharp inflection point close to the top  $L_s$ . The same inflection point was also observed above the top of the  $L_s$  in Configuration 1 (Cases 1 and 2) of Figs. 4(a) and 4(b). However, the rise in velocities above the short layer was compensated for by the taller layer, which acts as a second layer and hence uniform velocities were observed on the downstream side of the vegetation patch. The velocity structure within the vegetation patch was different at the three considered depths. In Configuration 1 (Cases 1 and 2) as shown in Figs. 4(a) and 4(b) at depth ( $Z/h_1 = 0.7$ ), the streamwise velocities within the first  $L_s$  and second  $L_t$  were low. The low velocities in the first  $L_s$  were due to the dense arrangement of short submergent vegetation, and the impact of these low velocities leads to the second  $L_t$ , and hence a uniform pattern of low velocities was observed in both layers. When the depth was further increased, i.e. ( $Z/h_1 = 1$ ), the streamwise velocities were a little higher near the top of the first short layer, but the velocities abruptly increased in the second tall layer compared to the first short layer. The increased velocities were due to the sparse arrangement of the  $L_t$  that gave less resistance to the flow. Finally, at the depths  $Z/h_1 = 1.2, 1.4$ , the velocity structure behavior gained an increasing pattern in both layers  $L_s$  and  $L_t$ . The increment in velocities

above the first  $L_s$  was due to the absence of any direct resistance in the path of flow, and maximum velocities were observed above the top of  $L_s$ , while the velocities were also increased in the second  $L_t$  due to the presence of less resistance and a sparse arrangement of tall vegetation layer.

When the position of layers was changed, i.e. in Configuration 2 (Cases 3 and 4) shown in Figs. 4(c) and 4(d) at depth  $Z/h_1 = 0.7$ , the velocities were higher in  $L_t$  and were lower in  $L_s$ . This means that the velocities were significantly changed by changing the position of  $L_s$  as a second layer and  $L_t$  as a first layer. Configuration 2 was ineffective in lowering velocities inside  $L_t$  as compared to Configuration 1. However, it was effective in the second  $L_s$  and the immediately downstream area at depth  $Z/h_1 = 0.7$ . When the depth was further increased, i.e. ( $Z/h_1 = 1$ ), the velocities further increased in the first layer ( $L_t$ ), and meanwhile, in the second layer ( $L_s$ ), velocities also gained an increment both at top of the short vegetation and the downstream region as well. Similarly, the same behavior of velocities was observed at depths  $Z/h_1 = 1.2$  and  $1.4$ . The higher velocities in the first  $L_t$  may promote erosion and increase the chance of tree breakage from the upstream side, whereas the second  $L_s$ , which was placed on the downstream side, may not trap the debris and broken trees significantly. A study by [Samarakoon et al. \[2012\]](#) suggests that introducing the short submerged vegetation (*P. odoratissimus*) as the front vegetation layer is efficient in reducing the drawbacks of the open gaps (like a road) in existing tall vegetation (*C. equisetifolia*) forests. Furthermore, multiple prior studies [[Tanaka et al., 2007, 2010](#); [Thuy et al., 2009](#)] found that planting *P. odoratissimus* in front of *C. equisetifolia* gave better tsunami protection. In this study, Configuration 1 effectively reduced the velocity within the vegetation, while the second tall layer played an important role in minimizing the increased velocities above the top of the short layer. According to [Tanaka et al. \[2009\]](#), the tall emergent vegetation placed after the short dense vegetation layer was able to trap the floating objects and broken branches.

### 3.1.2. Formation of shear layer at top of short vegetation layer

The contour plots of streamwise velocity distribution along Sec. 1 are presented in Figs. 5(a)–5(d). The  $x$  axis represents the longitudinal distance  $X$  of the domain, whereas the  $z$  axis depicts the vertical distance of the domain ( $Z/h_1$ ) normalized by the height of the short submergent trees ( $h_1$ ). When the flow approaches the vegetative area, it shows significant differences. In horizontal double vegetation HDLV model flows, a considerable spike in velocities, as well as an inflection point, was noted towards the top of the short submergent vegetation layer, i.e.  $1 < z/h_1 < 1.2$  and  $1 < z/h_1 < 1.4$  in Figs. 5(a)–5(d). The numerical model successfully captured the inflection point in the contour plots of streamwise velocity above  $L_s$ . It was due to the exchange of strong momentum between the top of  $L_s$  and the overlying flow. This zone is known as the shear zone. A velocity gradient developed across the mixing-layer zone toward the top of  $L_s$ . This mixing layer zone has the maximum intensity of vortices [[Singh et al., 2019](#)]. The pattern of velocities remained constant and low

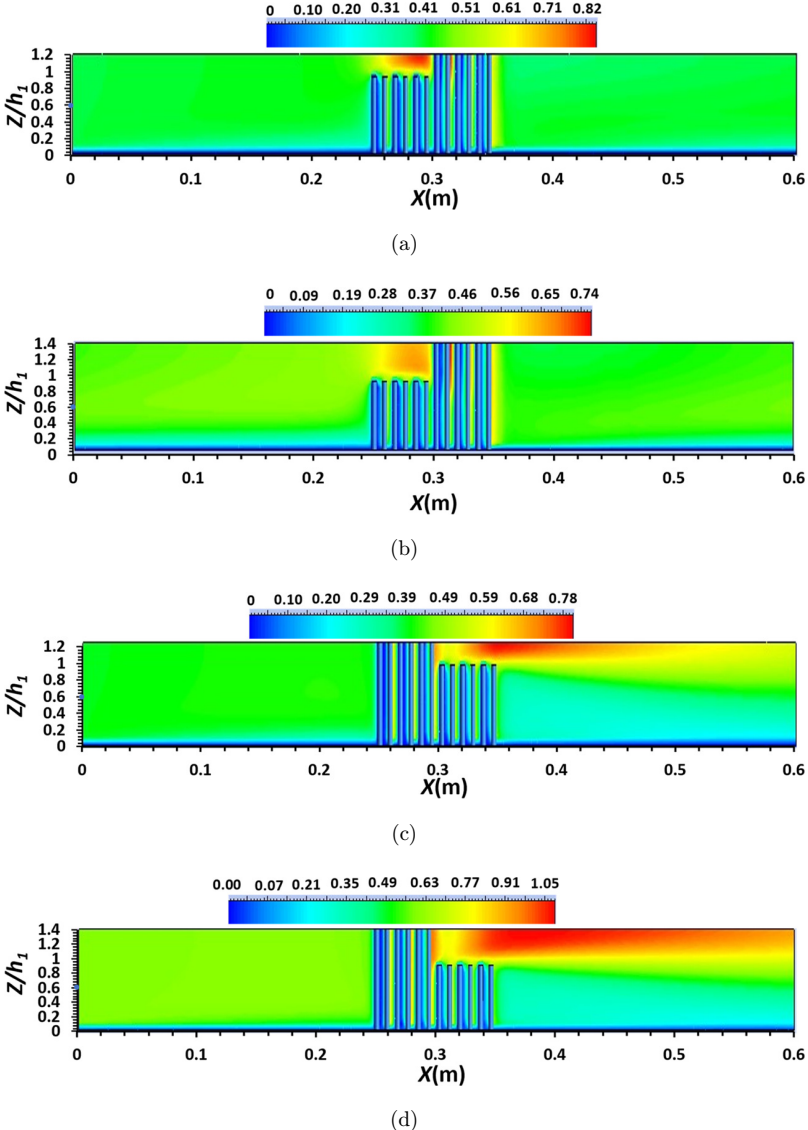


Fig. 5. The contour plots of streamwise velocities profiles along Sec. 1. (a) Case 1, (b) Case 2, (c) Case 3, and (d) Case 4.

under the mixing layer zone, i.e. below the short vegetation height ( $Z/h_1 < 1$ ). The fall in streamwise velocity below  $L_s$ , i.e. ( $Z/h_1 < 1$ ) was predominantly due to the drag offered by the dense vegetation arrangement, resulting in an inflection point in the velocity profiles. This sharp inflection behavior towards the top of  $L_s$  is identical to what has been reported in previous findings for submerged layered vegetation

flows [Righetti and Armanini, 2002; Lopez and Garcia, 2001] and VDLV flows [Anjum *et al.*, 2018; Rashedunnabi and Tanaka, 2018; Ghani *et al.*, 2019a].

In vegetation Configuration 1 (Cases 1 and 2), the contour plot of velocity shows that the formation of a shear layer zone due to inflection near the top of  $L_s$  is hindered by the  $L_t$  as a second layer. As a result of the drag generated by the  $L_t$ , the velocity gradient became less steep, preventing the creation of a shear zone downstream of the vegetation patch. On other hand, in Configuration 2 (Cases 3 and 4), the velocity profile above the top of the  $L_s$  encounters the strong shear layer zone and is not restricted due to the absence of  $L_t$ . Therefore, the length of the shear zone expands and intensifies up to the downstream side of the vegetation area. Furthermore, when the flow depth was high, as in Configuration 1 (Case 2) and Configuration 2 (Case 4), the shear layer zone over the top of the  $L_t$  became higher, and the length of the shear layer grew as well, especially in Case 4 compared to the low flow depth value (Cases 1 and 3). As a result of increasing the flow depth above the  $L_s$ , the velocity structure becomes even more complicated.

### 3.2. Contour plot distribution of velocities

#### 3.2.1. Lateral distribution of streamwise velocities

The computed contour plots of streamwise velocity ( $u$ ) along lateral Sec. 2 (upstream of vegetation), Sec. 3 (between the interface of two vegetation layers, i.e.  $L_s$  and  $L_t$ ), and Sec. 4 (downstream of the vegetation area) for Cases 1 and 3 are presented in Figs. 6(a)–6(f). The  $x$  axis represents the width of the channel (denoted by  $Y$ ), whereas the  $y$  axis shows the depth of the channel (denoted by  $Z/h_1$ ) normalized by the height of the short submergent vegetation layer. The streamwise velocities were extremely low in both instances (1 and 3) and fell to a minimum close to the bed for all the sections investigated (2, 3, 4) as shown in Figs. 6(a)–6(f). This was due to the resistance offered by the bed. As the flow approached the upstream side of the vegetation area in Configuration 1 (Case 1) at Sec. 1, the streamwise velocities were low within the short vegetation layer  $L_s$  ( $Z/h_1 < 1$ ) in Case 1, Fig. 6(a). This was due to its dense arrangement and the drag induced by vegetation cylinders, whereas the velocity magnitudes were higher above the  $L_s$ , i.e.  $Z/h_1 > 1$ , due to the absence of resistance offered by the short cylinders. Similarly, as the flow approached the upstream side of the vegetation area in Configuration 2 (Case 3) at Sec. 1 shown in Fig. 6(d), a uniform distribution of velocities was obtained due to the constant drag provided within the  $L_t$  from the bed to the top, and the magnitudes were high compared to Configuration 1 (Case 1) at the same Sec. 1. Furthermore, when the flow approached the middle of the vegetation area, i.e. Sec. 3 (interface between the vegetation layers  $L_s$  and  $L_t$ ), by considering Configuration 1 (Case 1) in Fig. 6(b). The velocities below the depth ( $Z/h_1 < 1$ ) became very slow compared to Sec. 1 due to the continuous resistance provided by the  $L_s$ , whereas above the depth ( $Z/h_1 > 1$ ), the velocities were higher in front of the gaps between the tall cylinders but lower in the region in front of the individual tall cylinders. Similarly, considering

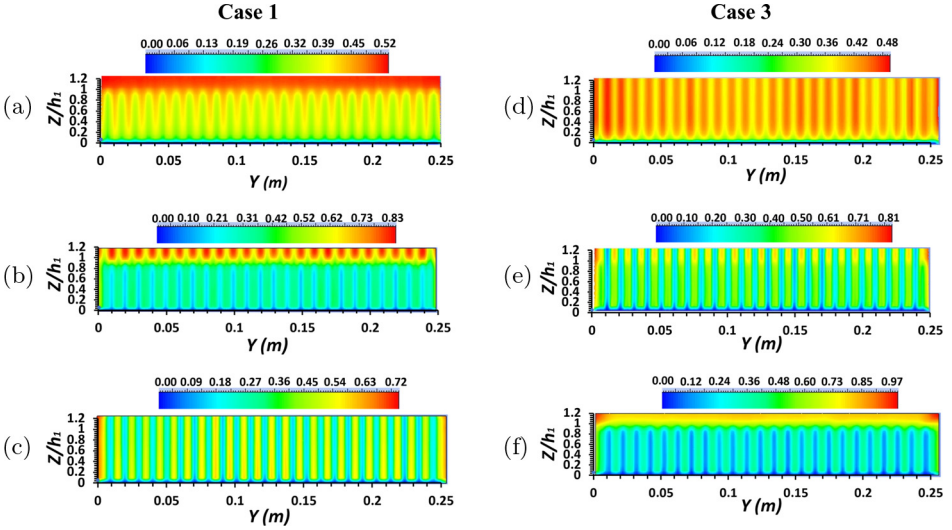


Fig. 6. Lateral contour plots of streamwise velocity. (a) Sec. 2, Case 1, (b) Sec. 3, Case 1, (c) Sec. 4, Case 1, (d) Sec. 2, Case 3, (e) Sec. 3, Case 3, and (f) Sec. 4, Case 3.

Configuration 2 (Case 3) at the same Sec. 2 in Fig. 6(e), the same velocity structure was observed in Configuration 1 (Case 1). However, the rise in velocities above the depth ( $Z/h_1 > 1$ ) in front of the gap region between the tall cylinders was low as compared to the Configuration 1 (Case 1) in Fig. 6(b). Finally, when the flow reached the downstream side of the vegetation area at Sec. 4 in Fig. 6(c), a uniform distribution of velocity was obtained at the back of the tall vegetation layer from the bed to the top ( $0 < Z/h_1 < 1.2$ ). Here, the magnitudes of velocities were high in the gap region between the spacing of the tall cylinders and low in the front region of individual tall cylinders  $L_t$ , whereas, at the same Sec. 4, the velocity magnitudes became very low at the back of the short vegetation layer and became high above the overlying fast-moving flow, consistent with Fig. 5(c).

### 3.2.2. Lateral distribution of lateral velocities

The contour plots of lateral velocities ( $v$ ) along Secs. 2–4 for Cases 1 and 3, respectively, are depicted in Fig. 7. Negative and positive values of lateral velocities inside the  $L_s$  and  $L_t$  are observed along Secs. 2–4, respectively. The positive and negative values represent the strong flow deflection at the sides of cylinders. Anjum and Tanaka [2019b] also observed similar behaviors of transverse velocities through vertically double-layer vegetation. The lateral velocities ( $v$ ) are larger inside the  $L_s$  ( $Z/h_1 < 1$ ) (Secs. 2 and 3 in Case 1 in Figs. 7(a) and 7(b) and Secs. 3 and 4 in Case 3 in Figs. 7(e) and 7(f) as compared to the  $L_s$  (i.e.  $Z/h_1 > 1$ ). It was caused by the strong lateral movement of particles due to retardations of the dense short layer ( $L_s$ ). The vegetation density has a significant impact on flow deflection [Anjum and Tanaka, 2020a]. The present results are in line with the findings of Anjum and

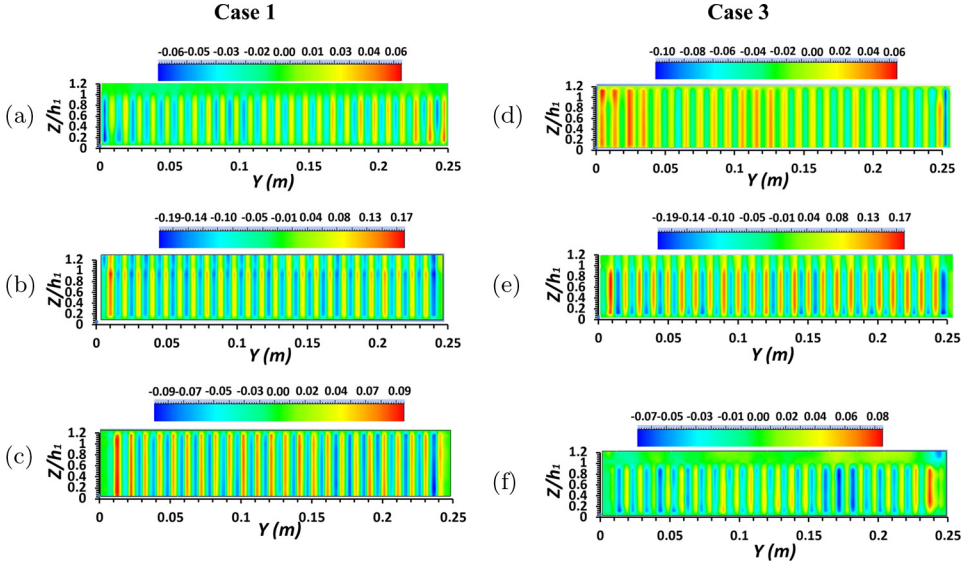


Fig. 7. Lateral contour plots of lateral velocity. (a) Sec. 2, Case 1, (b) Sec. 3, Case 1, (c) Sec. 4, Case 1, (d) Sec. 2, Case 3, (e) Sec. 3, Case 3, and (f) Sec. 4, Case 3.

Tanaka [2020b]; Zong and Nepf [2011]; Okamoto and Nezu [2013]. Furthermore, the lateral velocities became almost zero above the  $(L_s)Z/h_1 > 1$  in both Cases 1 and 3, which indicates that there was no lateral diversion of flow above the short submerged layer. The lateral velocities upstream of  $L_t$  (Sec. 2, Fig. 7(d)) in Case 3 and downstream of  $L_t$  (Sec. 4, Fig. 7(c)) in Case 1 are similar. Their plots remain almost constant up to the top of the free surface due to the continuous retardation by the tall cylinders. Anjum and Tanaka [2019b] also reported similar behavior. Due to the presence of small turbulence, a smaller fluctuation is observed in the velocity plot.

### 3.2.3. Lateral distribution of vertical velocities

Figure 8 presents the contour plot distribution of depth-wise ( $w$ ) velocities along Secs. 2–4 (for Cases 1 and 3). It is evident from the contour plots that the magnitude of the vertical velocities is very low as compared to the streamwise velocities. The vertical velocities showed a negative magnitude or close to zero along all sections in both Cases 1 and 3. A sharp inflection point in vertical/depth-wise velocities was visible near the top of the short layer ( $Z/h_1 = 1$ ) from the contour plots along Secs. 2 and 3 in Case 1 and along Secs. 3 and 4 in Case 3. The inflection behavior of vertical velocities near the top of the short layer indicates the depthwise movement of the flow [Anjum and Tanaka, 2019b]. This abrupt variation in depth-wise velocities occurred due to a momentum transfer between overlying flow layers. The depth-wise velocities become positive maximum above the  $L_s$  ( $Z/h_1 > 1$ ) at Sec. 2 (Case 1; Fig. 8(a)) and Sec. 3 (Case 3; Fig. 8(e)). Both these sections lie upstream of an  $L_s$  where the flow was deflected in an upward direction due to the resistance of a short

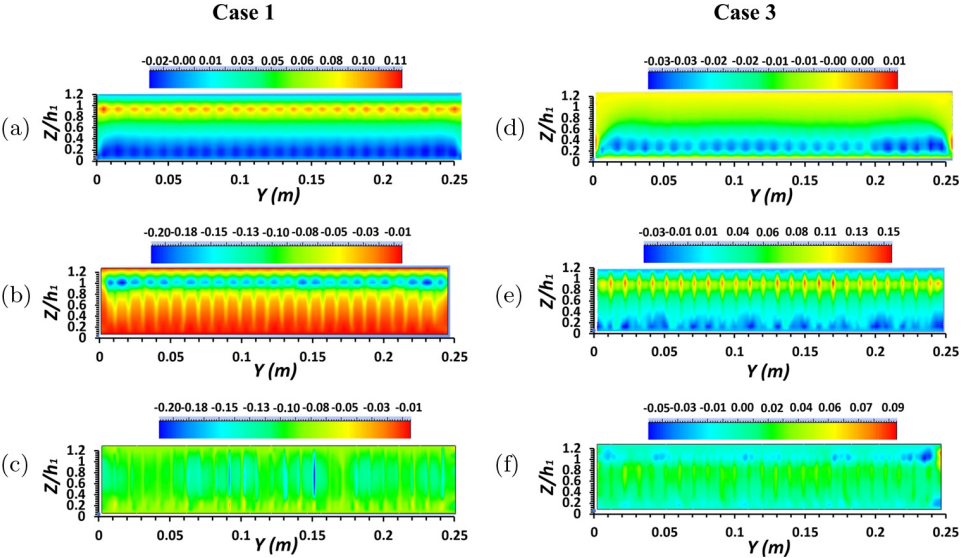


Fig. 8. Lateral contour plots of vertical velocity. (a) Sec. 2, Case 1, (b) Sec. 3, Case 1, (c) Sec. 4, Case 1, (d) Sec. 2, Case 3, (e) Sec. 3, Case 3, and (f) Sec. 4, Case 3.

submergent layer. In contrast, the depthwise velocities were negative near the top of the  $L_s$  ( $Z/h_1 = 1$ ) along Sec. 3 (Case 1) and Sec. 4 (Case 3). The negative magnitude of velocities is an indication of the downward flow [Anjum *et al.*, 2018]. Ghani *et al.* [2019b] also found that the maximum vertical movement of flow was observed near the top of short vegetations. The depth-wise velocities were very low or negative and almost constant along Sec. 4 in Cases 1 and 3, where the flow movement is downward.

### 3.3. Contour plots of velocity vectors

Figures 9 and 10 present the lateral distribution of secondary currents of streamwise velocity induced by the vegetation patch for Cases 1 and 3 (along Secs. 2–4). As discussed earlier, the inflection behavior in velocities above the  $L_s$  was observed. It was due to the drag of vegetation cylinders and momentum absorption by the vegetation which develops a mixing/strong shear layer at the interface of vegetation top and overlaying flow [Anjum and Tanaka, 2019a, b]. Thus, a high-velocity zone above the  $L_s$  and a low-velocity zone inside the  $L_s$  were generated which is the main cause of the Kelvin–Helmholtz instability [Finnigan, 2000; Ghisalberti and Nepf, 2005; Zhao and Huai, 2016]. These secondary currents originated from the difference in velocities between vegetated and non-vegetated zones and tend to move from a high-velocity zone to a low-velocity zone. In both cases, the strength and magnitude of secondary currents are maximum at the vertical interface (between the top boundary of short cylinders and overlaying flow) and the lateral interface (between vegetation cylinders and free-flow region, etc., gap region) as shown in Figs. 9 and 10, respectively.

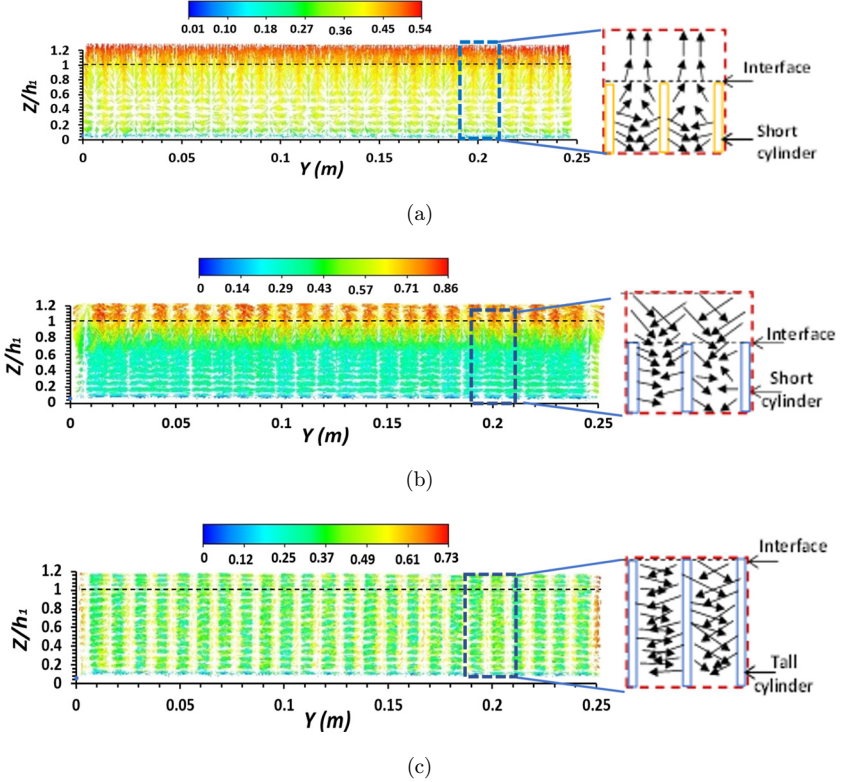


Fig. 9. Secondary currents of streamwise velocities during Case 1. (a) Sec. 2, (b) Sec. 3, and (c) Sec. 4.

Downward-moving clockwise and counterclockwise velocity currents are generated due to the lateral interface between the cylinders and the gap inside the short vegetations. Their strength inside the gap region (the region between the cylinders) is higher. These tend to move in the upward direction with higher intensity and strength near the top of the short vegetation layer due to the momentum transportation at the vertical interface between overlaying flow and vegetation top, as shown in Sec. 2 (Case 1) in Fig. 9(a). Contrarily, the direction of velocity currents was almost all downward due to continuous resistance of tall cylinders along Secs. 3 and 4 (Case 1) in Figs. 9(b) and 9(c). In contrast, the behavior of velocity currents was different in Case 3 from Case 1 due to the changing positions of  $L_t$  and  $L_s$ . Clockwise and counterclockwise velocity currents in the downward direction were observed along Sec. 2 (Case 3, Fig. 10(a)). In contrast, their direction becomes upward near the top of  $L_s$  along Sec. 3 (Case 3, Fig. 10(b)) due to the absence of resistance of  $L_t$ .

### 3.4. Reynolds stresses

The Reynolds normal ( $u'u'$ ;  $u'$  indicates variation in the streamwise direction of a velocity component) of the computational model was determined to investigate the

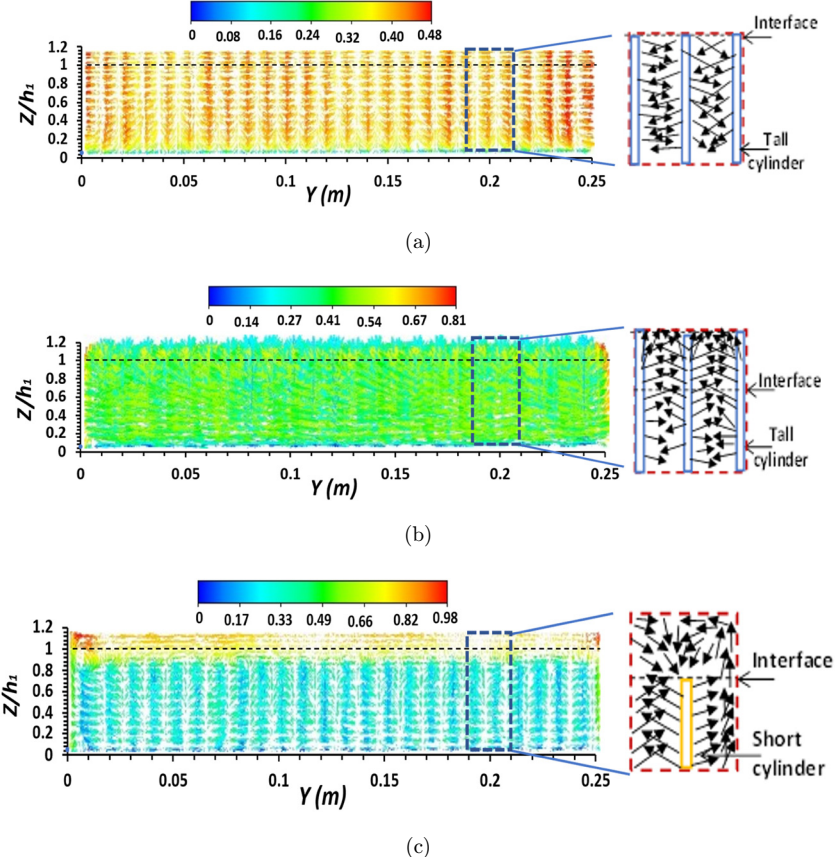


Fig. 10. Secondary currents of streamwise velocities during Case 3 (a) Sec. 2, (b) Sec. 3, and (c) Sec. 4.

turbulence characteristics. The contour plots and vertical profiles of the computed Reynolds normal stresses at different specified locations are presented in Figs. 11 and 12, respectively. In Fig. 11, the  $x$  axis depicts the Reynolds stresses normalized by  $U^2$ , while the  $y$  axis represents the flow depth, which was normalized by  $h_1$  (shorter vegetation height) in vertical profiles.

The vertical profiles of Reynolds normal stresses at specified locations showed that the Reynolds stresses were almost constant from the bed to the tops of cylinders at those locations lying upstream (location 1) and inside (location 2) the  $L_t$  in Case 3 (Figs. 11(c) and 11(d)). Similarly, location 4 (inside the taller emergent layer) and location 5 (downstream of  $L_t$ ) in Case 1 also remained constant, as shown in Figs. 11(a) and 11(b). The plots of locations located inside and directly downstream of the  $L_s$  (locations 2 and 3 in Case 1; locations 3–5 in case 3) consist of three different behaviors (Fig. 11). The normal stresses are very low (at locations 2 and 3) in Case 1 (Figs. 11(a) and 11(b)) during the first portion of the plot near the bed up to a specific flow depth. In contrast, these stresses are higher (at locations 3–5) near the

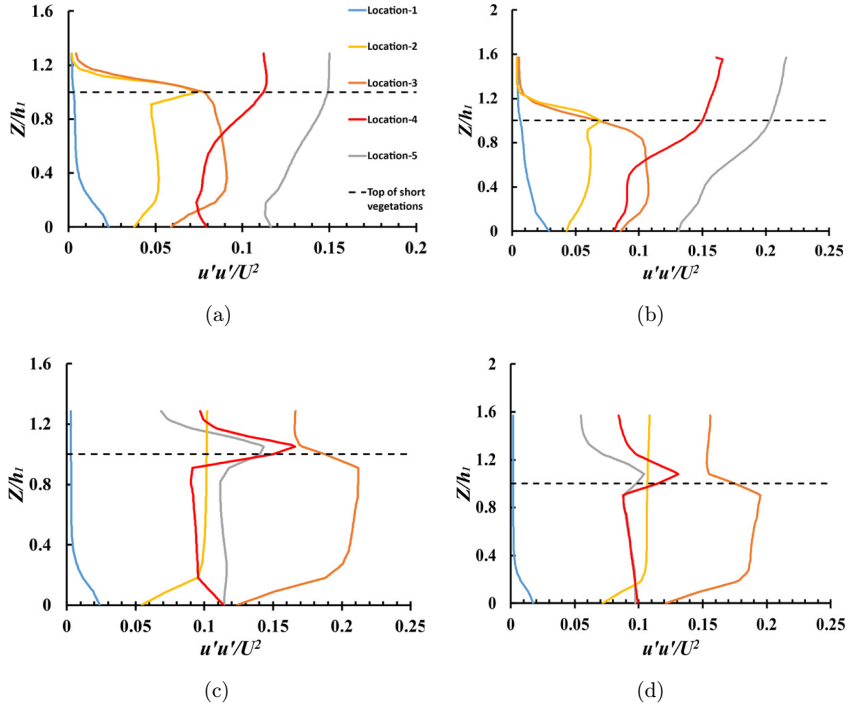


Fig. 11. Secondary currents of stream-wise velocities during Case 3. (a) Sec. 2, (b) Sec. 3, and (c) Sec. 4.

bed up to a certain depth in Case 3 (Figs. 11(c) and 11(d)). In the plot's second zone, these stresses become constant before the top of vegetations in both Cases 1 and 3. In the third zone of the plot, inflection points occur where sharp variation is visible near the top of vegetation  $Z/h_1 = 1$  due to the exchange of momentum between flow layers [Finnigan, 2000; Ghani *et al.*, 2019b]. They also reported that the sharp inflection behavior in Reynolds normal stresses was more prominent near the top of vegetation.

The contour plots of Reynolds normal stresses (on the bed) (Fig. 12) showed that the normal stresses are relatively minimum downstream of  $L_t$  in Cases 1 and 2 (Figs. 12(a) and 12(b)), while they were maximum inside the  $L_s$  in Cases 3 and 4 (Figs. 12(c) and 12(d)). The secondary flow was generated inside the gap region (the region between the cylinders) where the stresses were maximum compared to the direct upstream and downstream of the cylinders. It indicates that the flow was highly turbulent due to the strong influence of vegetation at these locations. The higher turbulence downstream and inside the vegetations will be favorable for sediment transportation. In contrast, the Reynolds stresses are approximately negligible upstream of the vegetation patch. It shows that turbulence characteristics upstream were not considerably affected by vegetation. Qu *et al.* [2020] found that emergent vegetation plays an important role in sediment deposition, whereas sediment

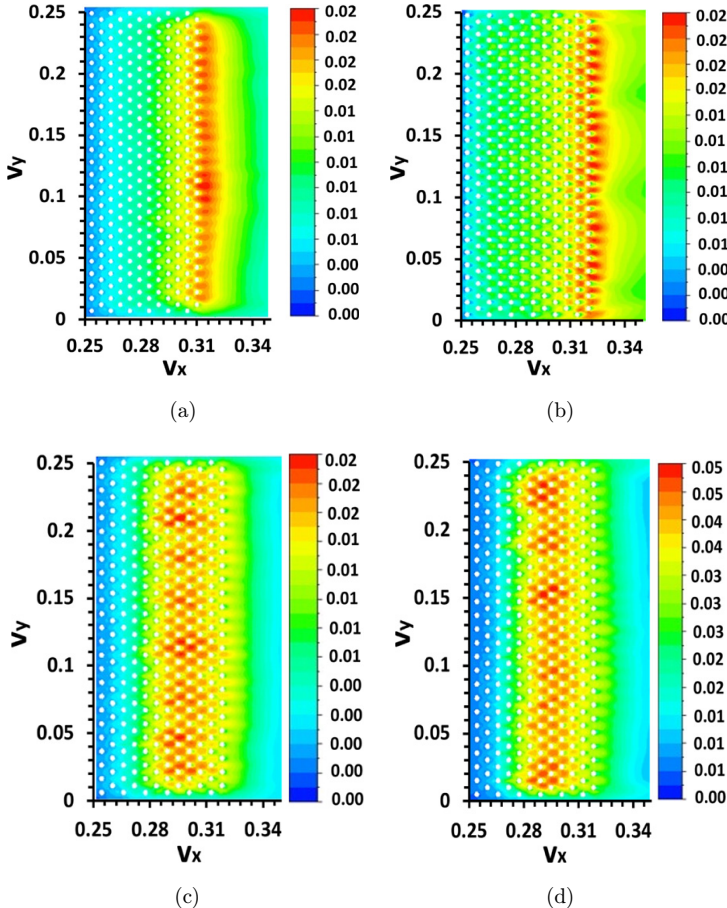


Fig. 12. Contour plot distribution of bed normal stresses ( $u'u'$ ) (a) Case 1, (b) Case 2, (c) Case 3, and (d) Case 4.

transportation mainly occurred above the submerged vegetation. In this study, the downstream layer ( $L_t$ ) in Configuration 1 (Cases 1 and 2) would be more favorable for sediment deposition. In contrast, the sediment transportation and scouring directly downstream of the ( $L_s$ ) in Configuration 2 (Cases 3 and 4) may cause a great risk to the vegetation structure.

#### 4. Conclusions

The flow characteristics through HDLV during the inland tsunami flows (under critical flow conditions) were numerically examined with two different configurations of short submergent and tall emergent layers of vegetation. The RSM successfully captured the flow characteristics including detailed streamwise, transverse, and

vertical velocity structures and the distribution of Reynolds stresses at specified locations. The main findings acquired from this study are as follows:

- In both vegetation Configurations 1 and 2, the mean streamwise velocity profile consisted of a sharp inflection point near the top of the short submergent layer ( $L_s$ ). A 79–87% increment in streamwise velocities was noted above the short vegetations ( $Z/h_1 > 1$ ) as compared to inside the vegetation ( $Z/h_1 < 1$ ) in Configurations 1 and 2, respectively. This was due to the maximum generation of vortices which gives rise to the momentum transfer between the overlying flow and top of the short submergent layer ( $L_s$ ) and indicates a velocity gradient in this zone.
- The difference between the streamwise velocities inside the tall emergent layer ( $L_t$ ) between zone  $Z/h_1 < 1$  and  $Z/h_1 > 1$  was not significant; it was only 5–16% in both Configurations 1 and 2. It was due to continuous retardation by the tall layer up to the free surface.
- In both Configurations 1 and 2, a shear layer was generated above the short submergent layer; however, in Configuration 1, the downstream tall emergent layer, as a second layer, confined this shear layer to the region directly above the short layer. In Configuration 2, the tall emergent layer served as the first layer, and therefore, this shear layer was extended to the downstream region due to the absence of any hindrance. Furthermore, as the flow depth rose, the shear layer became more intense and longer.
- The magnitude of lateral velocities was extremely low, with positive and negative values within the vegetation layers, owing to a minor movement of flow in the lateral direction. While lateral velocities most often tended to zero above the short submergent layer ( $L_s$ ), this indicates that there was no lateral movement of flow above the short layer. Similarly, the maximum positive and negative vertical velocities were found towards the top of the short submergent layer, indicating upward and downward flow movement in this area.
- The vertical profiles of Reynolds normal stresses revealed that they were almost constant inside the tall layer up to the top of the free surface, while a sharp inflection in stresses was seen at the top of the short layer in both Configurations 1 and 2. However, the bed stresses were higher in the short submergent layer in Configuration 2 than in the tall submergent layer in Configuration 1.

This study investigated the effectiveness of a horizontal double layer of vegetation HDLV consisting of short and tall layers as a countermeasure against inland tsunami flows. The results of this study revealed that both vegetation Configuration 1 (with a short layer as the first layer and a tall layer as the second layer) and Configuration 2 (with a tall layer as the first layer and a short layer as the second layer) were efficient for velocity attenuation purposes. However, Configuration 1 performed relatively better than Configuration 2 because the short submergent layer as the first layer reduced the velocity within the vegetation, while the tall emergent layer as a second

layer played a pivotal role in diminishing the increased velocities and limiting the shear layer above the short submergent layer. Hence, the tall emergent layer as a second layer in Configuration 1 may be advantageous for sediment deposition and trapping debris and broken branches. In Configuration 2, the short submergent layer as the second layer produced a stronger shear layer with greater velocities above the short submergent layer, which was not appropriate for the downstream area.

Hence, Configuration 1 could be more beneficial as a defense for inland regions against a devastating tsunami than Configuration 2. In the future, the detailed behavior and impact of external flow structures, such as free surface level fluctuations and other flow characteristics, should be investigated by analyzing additional parameters such as vegetation heights and density.

## References

- Anjum, N. and Tanaka, N. [2019a] "Experimental study on flow analysis and energy loss around discontinued vertically layered vegetation," *Environ. Fluid Mech.* **20**, 791–817.
- Anjum, N. and Tanaka, N. [2019b] "Numerical investigation of velocity distribution of turbulent flow through vertically double-layered vegetation," *Water Sci. Eng.* **12**(4), 319–329.
- Anjum, N. and Tanaka, N. [2020a] "Hydrodynamics of longitudinally discontinuous vertically double layered and partially covered rigid vegetation patches in open channel flow," *River Res. Appl.* **36**(1), 115–127.
- Anjum, N. and Tanaka, N. [2020b] "Investigating the turbulent flow behaviour through partially distributed discontinuous rigid vegetation patches in open channel flow," *River Res. Appl.* **36**(8), 1701–1716, doi/10.1002/rra.3671.
- Anjum, N., Ghani, U., Pasha, G. A., Latif, A., Sultan, T. and Ali, S. [2018] "To investigate the flow structure of discontinuous vegetation patches of two vertically different layers in an open channel," *Water* **10**(1), 75.
- Danielsen, F., Sorensen, M. K., Olwig, M. F., Selvam, V., Parish, F., Burgess, N. D., Hiraishi, T., Karunagaran, V. M., Rasmussen, M. S., Hansen, L. B., Quarto, A. and Suryadiputra, N. [2005] "The Asian tsunami: A protective role for coastal vegetation," *Science* **310**, 643.
- Finnigan, J. [2000] "Turbulence in plant canopies," *Annual Rev. Fluid Mech.* **32**(1), 519–571.
- Fritz, H. M., Borrero, J. C., Synolakis, C. E. and Yoo, J. [2006] "2004 Indian Ocean tsunami flow velocity measurements from survivor videos," *Geophys. Res. Lett. L* **33**, 24605.
- Ghani, U., Anjum, N., Pasha, G. A. and Ahmad, M. [2019a] "Investigating the turbulent flow characteristics in an open channel with staggered vegetation patches," *River Res. Appl.* **35**(7), 966–978.
- Ghani, U., Anjum, N., Pasha, G. A. and Ahmad, M. [2019b] "Numerical investigation of the flow characteristics through discontinuous and layered vegetation patches of finite width in an open channel," *Environ. Fluid Mech.* **19**(6), 1469–1495.
- Harada, K. and Kawata, Y. [2005] "Study on tsunami reduction effect of coastal forest due to forest growth," *Ann. Disaster Prev. Res. Inst.* **48C**, 161–165.
- Imura, K. and Tanaka, N. [2012] "Numerical simulation estimating the effects of tree density distribution in coastal forest on tsunami mitigation," *Ocean Eng.* **54**, 223–232.
- Irtem, E., Gedik, N., Kabdasli, M. S. and Yasa, N. E. [2009] "Coastal forest effects on tsunami run-up heights," *Ocean Eng.* **36**, 313–320.
- Jayatissa, L. P., Dahdouh-Guebas, F. and Koedam, N. [2002] "A review of the floral composition and distribution of mangroves in Sri Lanka," *Bot. J. Linn. Soc.* **138**, 29–43.

- Kathiresan, K. and Rajendran, N. [2005] "Coastal mangrove forests mitigated tsunami," *Estuar. Coast. Shelf Sci.* **65**(3), 601–606.
- Liu, D., Diplas, P., Hodges, C. C. and Fairbanks, J. D. [2010] "Hydrodynamics of flow through double layer rigid vegetation," *Geomorphology* **116**(3–4), 286–296.
- Lopez, F. and Garcia, M. H. [2001] "Mean flow and turbulence structure of open channel flow through non-emergent vegetation," *J. Hydraul. Eng.* **127**(5), 392–402.
- Mori, N. and Takahashi, T. [2012] "Nationwide post event survey and analysis of the 2011 Tohoku earthquake tsunami," *Coast. Eng. J.* **52**(1), 1250001.
- Okamoto, T. and Nezu, I. [2013] "Spatial evolution of coherent motions in finite-length vegetation patch flow," *Environ. Fluid Mech.* **13**, 417–434.
- Osti, R., Tanaka, S. and Tokioka, T. [2009] "The importance of mangrove forest in tsunami disaster mitigation," *Disasters* **33**(2), 203–213.
- Pasha, G. A. and Tanaka, N. [2017] "Undular hydraulic jump formation and energy loss in a flow through emergent vegetation of varying thickness and density," *Ocean Eng.* **141**, 308–325.
- Qu, G., Yao, S., Ding, B., Pan, S., Hu, C. and Liu, F. [2020] "Experimental study on the mechanisms of flow and sediment transport in a vegetated channel," *Water Manag.* **173**, 249–264.
- Rashedunnabi, A. H. M. and Tanaka, N. [2018] "Physical modelling of tsunami energy reduction through vertically two layered rigid vegetation," *Proc. 12th Int. Symp. Ecohydraulics*, Tokyo, p. 1e10.
- Rashedunnabi, A. H. M. and Tanaka, N. [2019] "Energy reduction of a tsunami current through a hybrid defense system comprising a sea embankment followed by a coastal forest," *Geosciences* **9**, 247.
- Rashedunnabi, A. H. M. and Tanaka, N. [2020] "Effectiveness of double-layer rigid vegetation in reducing the velocity and fluid force of a tsunami inundation behind the vegetation," *Ocean Eng.* **201**, 107142.
- Righetti, M. and Armanini, A. [2002] "Flow resistance in open channel flows with sparsely distributed bushes," *J. Hydrol.* **269**(1–2), 55–64.
- Roulund, A., Sumer, B. M., Fredsøe, J. and Michelsen, J. [2005] "Numerical and experimental investigation of flow and scour around a circular pile," *J. Fluid Mech.* **534**, 351–401.
- Samarakoon, M. B., Tanaka, N. and Iimura, K. [2012] "Improvement of effectiveness of existing *Casuarina equisetifolia* forests in mitigating tsunami damage," *J. Environ. Manag.* **114**, 105–114.
- Singh, P., Rahimi, H. R. and Tang, X. [2019] "Parameterization of the modelling variables in velocity analytical solutions of open-channel flows with double-layered vegetation," *Environ. Fluid Mech.* **19**(3), 765–784.
- Takemura, T. and Tanaka, N. [2007] "Flow structures and drag characteristics of a colony type emergent roughness model mounted on a flat plate in uniform flow," *Fluid Dyn. Res.* **39**, 694–710.
- Tanaka, N. [2009] "Vegetation bioshields for tsunami mitigation: Review of the effectiveness, limitations, construction, and sustainable management," *Lands Ecol. Eng.* **5**, 71–79.
- Tanaka, N. and Onai, A. [2017] "Mitigation of destructive fluid force on buildings due to trapping of floating debris by coastal forest during the Great East Japan tsunami," *Landsc. Ecol. Eng.* **13**, 131–144.
- Tanaka, N., Jinadasa, K. B. S. N., Mowlood, M. I. M. and Fasly, M. S. M. [2010] "Coastal vegetation planting projects for tsunami disaster mitigation: Effectiveness evaluation of new establishments," *Landsc. Ecol. Eng.* **7**, 127–135.

- Tanaka, N., Nandasena, N. A. K., Jinadasa, K. B. S. N., Sasaki, Y., Tanimoto, K. and Mowjood, M. I. M. [2009] “Developing effective vegetation bioshield for tsunami protection,” *Civil Eng. Environ. Syst.* **26**, 163–180.
- Tanaka, N., Sasaki, Y., Mowjood, M. I. M., Jinadasa, K. B. S. N. and Homchuen, S. [2007] “Coastal vegetation structures and their functions in tsunami protection: Experience of the recent Indian Ocean tsunami,” *Lands. Ecol. Eng.* **3**, 33–45.
- Tanaka, N., Yagisawa, J. and Yasuda, S. [2013] “Breaking pattern and critical breaking condition of Japanese pine trees on coastal sand dunes in huge tsunami caused by Great East Japan Earthquake,” *Nat. Hazards* **65**, 423–442.
- Tanaka, N., Yasuda, S., Iimura, K. and Yagisawa, J. [2014] “Combined effects of coastal forest and sea embankment on reducing the washout region of houses in the Great East Japan tsunami,” *J. Hydro-Environ. Res.* **8**, 270–280.
- Thuy, N. B., Tanimoto, K., Tanaka, N., Harada, K. and Iimura, K. [2009] “Effect of open gap in coastal forest on tsunami run-up-investigations by experiment and numerical simulation,” *Ocean Eng.* **36**, 1258–1269.
- Thuy, N. B., Tanimoto, K. and Tanaka, N. [2010] “Flow and potential force due to runup tsunami around a coastal forest with a gap - experiments and numerical simulations,” *Sci. Tsunami Hazards* **29**(2), 43–69.
- Thuy, N. B., Nandasena, N. A. K., Dang, V. H. and Tanaka, N. [2018] “Simplified formulae for designing coastal forest against tsunami run-up: One-dimensional approach,” *Nat. Hazards* **92**, 327–346.
- Wang, W., Huai, W. X. and Gao, M. [2014] “Computation of flow structure through double layer vegetation,” *Proc. Mathematical and Computational Methods in Science and Engineering*, p. 132e136.
- Wolanski, E., Jones, M. and Bunt, S. J. [1980] “Hydrodynamics of a tidal creek-mangrove swamp system,” *Aust. J. Marine Freshwater Res.* **31**, 431–450.
- Yanagisawa, H., Koshimura, S., Goto, K., Miyagi, T., Imamura, F., Ruanggrassamee, A. and Tanavud, C. [2009] “The reduction effects of mangrove forest on a tsunami based on field surveys at Pakarang Cape, Thailand and numerical analysis,” *Estuar. Coast. Shelf Sci.* **81**, 27–37.
- Yanagisawa, H., Koshimura, S., Miyagi, T. and Imamura, F. [2010] “Tsunami damage reduction performance of a mangrove forest in Banda Aceh, Indonesia inferred from field data and a numerical model,” *J. Geophys. Res.* **115**, C06032.
- Zhao, F. and Huai, W. [2016] “Hydrodynamics of discontinuous rigid submerged vegetation patches in open-channel flow,” *J. Hydro-Environ. Res.* **12**, 148–160.
- Zong, L. and Nepf, H. M. [2011] “Vortex development behind a finite porous obstruction in a channel,” *J. Fluid Mech.* **691**, 368–391.